Investigation of the mechanical behavior of kangaroo humeral head cartilage tissue by a porohyperelastic model based on the strain-rate-dependent permeability

Namal Thibbotuwawa[1], Adekunle Oloyede[1], Wijitha Senadeera[1], Tong Li[1] and YuanTong Gu[1]*

[1]School of Chemistry, Physics and Mechanical Engineering, Queensland University of Technology, Brisbane, Australia.

*Corresponding Author: Prof. YuanTong Gu

School of Chemistry, Physics and Mechanical Engineering,

Queensland University of Technology,

GPO Box 2434, Brisbane, QLD 4001, Australia

Email: yuantong.gu@qut.edu.au

Tel: +61-7-31381009

Fax: +61-7-31381469

Abstract

Solid-interstitial fluid interaction, which depends on tissue permeability, is significant to the strain-rate-dependent mechanical behavior of humeral head (shoulder) cartilage. Due to anatomical and biomechanical similarities to that of the human shoulder, kangaroos present a suitable animal model. Therefore, indentation experiments were conducted on kangaroo shoulder cartilage tissues from low (10^{-4}/s) to moderately high (10^{-2}/s) strain-rates. A porohyperelastic model was developed based on the experimental characterization; and a permeability function that takes into account the effect of strain-rate on permeability (strain-rate-dependent permeability) was introduced into the model to investigate the effect of rate-dependent fluid flow on tissue response. The prediction of the model with the strain-rate-dependent permeability was compared with those of the models using constant permeability and strain-dependent permeability. Compared to the model with constant permeability, the models with strain-dependent and strain-rate-dependent permeability were able to better capture the experimental variation at all strain-rates ($p<0.05$). Significant differences were not identified between models with strain-dependent and strain-rate-dependent permeability at strain-rate of 5×10^{-3}/s ($p=0.179$). However, at strain-rate of 10^{-2}/s, the model with strain-rate-dependent permeability was significantly better at capturing the experimental results ($p<0.005$). The findings thus revealed the significance of rate-dependent fluid flow on tissue behavior at large strain-rates, which provides insights into the mechanical deformation mechanisms of cartilage tissues.

2

1 Introduction

In physical activities, such as lifting and throwing, shoulder cartilages are subjected to physiologically different strain-rates. It is essential that the shoulder cartilage has the ability to undergo controlled deformation in response to these different external loading conditions, in order to reduce the risk of chondrocyte damage, extracellular matrix damage, and bone-to-bone contact in the joint. Solid-interstitial fluid interaction is considered to play an important role in facilitating this behavior of shoulder cartilage tissues. However, there is limited investigation on the strain-rate-dependent mechanical behavior of shoulder cartilage tissues. Nonetheless, it is crucial to understand the extent to which solid-interstitial fluid interaction facilitates strain-rate-dependent behavior of shoulder cartilage tissues, in order to identify its implications for the initiation of shoulder osteoarthritis and development of artificial shoulder cartilage tissues.

Evidence from the literature indicates that the mechanical behavior of articular cartilage is strain-rate-dependent (DiSilvestro et al., 2001; Langelier and Buschmann, 2003; Li et al., 2003; Li and Herzog, 2004; Oloyede and Broom, 1992; Oloyede et al., 1992). According to experimental findings, with increasing strain-rate, the stiffness of cartilage quickly increases at the beginning, and then approaches an asymptotic value (Edelsten et al., 2010; Oloyede et al., 1992). The interplay between solid and interstitial fluid contributes considerably to this behavior with 70%-80% of the load being supported by the matrix at low strain-rates (10^{-4}/s) (Oloyede and Broom, 1992), while the fluid contributes to a similar percentage at moderately large strain-rates (10^{-2}/s) (Li and Herzog, 2004; Oloyede and Broom, 1992). Although studies (Li et al., 2003; Oloyede and Broom, 1992) suggest that the loading velocity affects fluid behavior inside the tissue, there is a lack of studies investigating its effect on solid-interstitial fluid interaction. Loading cartilage from low to impact strain-rates, Oloyede et al. (1992) observed a poroelastic behavior at low strain-rates ($5x10^{-5}$/s) and elastic behavior at impact strain-rate (10^3/s). They claimed that the drag-forces introduced by the reduction of permeability and solid-interstitial fluid frictional-interactions largely contribute to the strain-rate-dependent behavior. Further investigations by Oloyede and Broom (1992) reported that the relationship

between effective matrix stress and pore pressure changes considerably when the strain-rate is increased from 10^{-3}/s to 10^{-2}/s. They claimed that there is a fundamental change in the deformation mechanism as the strain-rate increases, and that this could be due to fluid being increasingly contained inside the tissue with the increase in loading velocity.

The solid-interstitial fluid interaction of cartilage tissues is often investigated using finite element (FE) models due to experimental difficulties in investigating the tissue's internal behavior. For instance, Li et al. (2003) used a fibril-reinforced poroelastic FE model to investigate the strain-rate-dependent behavior of cartilage tissues from 5×10^{-4}/s to 5×10^{-2}/s. Their study indicated that fibril stiffening, determined by flow rates, which in turn may depend on strain-rate, contributes to stiffness increase of cartilage tissues with rate of loading. Direct fluid pressure measurement in Soltz and Ateshian's (2000) study has shown the important effect of fluid flow dependent drag-forces on cartilage tissue behavior under dynamic loading. Although there are evidences that the flow-independent viscoelasticity affects the strain-rate-dependent behavior of cartilage tissues at large strain-rates (DiSilvestro et al., 2001), whether the cartilage matrix possesses flow-independent viscoelasticity is still an ongoing investigation (Huang et al., 2001; Julkunen et al., 2013). Also, tension-compression nonlinearity of cartilage tissues along with flow-independent and flow-dependent viscoelastic mechanisms in combination have been used to improve model predictions at large strain-rates (Huang et al., 2001).

Although solid-interstitial fluid interaction is known to affect the tissue behavior, detailed investigation on its effect on strain-rate-dependent behavior is limited. Particularly there is no reported literature on the significant/insignificant nature of the strain-rate-dependent fluid flow on cartilage deformation behavior. Therefore, the current study mainly aims at investigating: 1) how the solid-interstitial fluid interaction facilitates the strain-rate-dependent behavior of shoulder cartilage tissues; and 2) whether the strain-rate-dependent fluid flow significantly affects the strain-rate-dependent behavior of shoulder cartilage tissues. In order to achieve these objectives, the paper firstly elaborates on the selection of an animal (kangaroo) model for shoulder cartilage studies. Then the biomechanical experiments conducted to understand the mechanical

4

behavior of kangaroos shoulder cartilage tissues is presented. The details of the porohyperelastic model are presented next, along with the introduction of strain-dependent permeability and strain-rate-dependent permeability. Subsequently, the paper discusses the findings by evaluating the suitability of the chosen animal model and the comparison of porohyperelastic models that include different permeability functions. These findings will provide insight into load bearing mechanisms of cartilage tissue from low to high strain-rates, as well as insight into changes in tissue behavior that have been observed in previous studies (Oloyede and Broom, 1992; Oloyede et al., 1992).

3 Experimental Methodology

3.1 The experimental animal model for shoulder cartilage

In selecting a suitable animal model for shoulder cartilage research, the shoulder joint of the animal model should be anatomically and biomechanically similar to that of a human's shoulder joint. In addition, sufficient tissue thickness is also required to conduct macroscale testing. Quadruped animals use forelimbs for weight bearing during movement. However, primates like humans do not regularly use the shoulder for weight bearing activities and can additionally move in more than one plane (Sonnabend and Young, 2009). These differences have important implications on the adaptation and architecture of shoulder cartilages (Longo et al., 2011)—in other words, their mechanical properties—suggesting the importance of choosing a suitable animal model. Apart from non-human primates, macropods, rats and certain types of mice (kangaroo mice, dipodids, springhare and hopping mice) have shoulder joints similar to those of humans. The rat is one of the most commonly used animal models for shoulder research because it is considered to have similar bone anatomy and overhead activity to that of the human shoulder (Longo et al., 2011). However, the small tissue thickness of its articular cartilage is a disadvantage in carrying out macroscale mechanical testing. On the other hand, there are ethical and economic concerns that limit the use of non-human primate tissues for testing purposes (Longo et al., 2011). Rare species, such as the tree kangaroo, also have very similar anatomy and biomechanics to that of the human shoulder (Sonnabend and Young, 2009). Recently, the kangaroo has been postulated as a potential animal model to study upper-limb joint cartilages

5

(He et al., 2013) due to a considerably lower loading experienced by upper-limb joints compared to lower-limb joints, similar to that of humans. Considering these factors, the kangaroo was considered as the most suitable animal model for shoulder cartilage research in the present study.

3.2 Physiological strain-rates and strains experienced by joints

There are number of earlier studies that have tested cartilage under different strain-rates. Radin et al. (1970) tested cartilage from 2.7×10^{-3}/s to 3.5×10^{-2}/s and Lai et al. (1981) loaded the cartilage from 3.3×10^{-5}/s to 3.3×10^{-4}/s. Investigating cartilage response for wide range of strain-rates, Oloyede et al. (1992) indented cartilage from 10^{-5}/s to 10^{3}/s. More recently Langelier and Buschmann (2003), DiSilvestro et al. (2001) and Li et al. (2003) studied cartilage in the range of 10^{-4}/s to 5×10^{-2}/s strain-rates. To authors knowledge there aren't any existing studies that have measured physiological strain-rates experienced by cartilages in vivo. However, maximum physiological strain-rate measured by Rubin and Lanyon (1982), attaching strain gages directly to radial and tibia mid shaft of dogs and horses, in a treadmill study, when animals are galloping was 8×10^{-2}/s. Also in another study (Farkas et al., 1987), where load cells were implanted on tibia of a rabbit approximately 1cm below the knee joint has reported stain-rates of 3×10^{-2}/s when impulse loads were applied on limbs. Therefore strain-rate in the order of 10^{-2}/s can be considered as at higher end of the physiological strain-rates.

The peak load of an impact on joints, which potentially causes tissue damage occurs in much less than a second after initial application of load (Quinn et al., 2001a; Thompson et al., 1993). For examples, motor car impact accidents, which occur in milliseconds, generally happens at around 10^{3}/s strain-rate (Finlay and Repo, 1979). Sub-impact loads occur in several seconds (in the order of 1/s strain-rates), and may induce surface cracks and chondrocyte death (Quinn et al., 2001a). Further, from reported in vivo deformation data on tibiofemoral joint, physiological strains on average can go up to 30%, ranging from approximately 10%-40% during daily activities (Bingham et al., 2008; Liu et al., 2010). Base on above information, in the current study, strain-rates ranging from 10^{-4}/s to 10^{-2}/s were chosen to cover physiological low and high ends of strain-rates and cartilage was loaded up to 30% strain to represent average loading in joint cartilages.

6

3.3 Tissue harvesting and preparation

Visually normal cartilage samples of 8 mm diameter with 2-3 mm of subchondral bone intact (Fig. 1a) were harvested using a specially designed, stainless steel puncher. The samples were obtained from the central load bearing area of the humeral head, from ten adult red kangaroos (approximately 5-years-old), bought from an abattoir within 24-hours of slaughter (Fig. 1b). After harvesting, samples were preserved in phosphate-buffered saline (PBS)-inhibitor solution that contains antibiotics (200mM L-glutamine, 10000 units of Penicillin and 10mg/mL of streptomycin; Sigma-Aldrich, Castle Hill, NSW) and were stored at -20°C (Qu et al., 2013). Before the subsequent biomechanical testing, samples were thawed for approximately 30 minutes in PBS at room temperature—i.e., approximately 27°C (Changoor et al., 2010). Samples went through a single freeze-thaw cycle so as to ensure that the mechanical properties and behavior of the tissues were not affected by multiple freeze-thaw cycles (Changoor et al., 2010; Qu et al., 2013).

3.4 Ultrasound thickness measurement

The ultrasound measurements were conducted using a 10MHz, Ø3mm plane-ended contact transducer (V129 Panametrics Inc., Massachusetts, USA). During these measurements, a 3mm distance was set between cartilage surface and transducer (Brown et al., 2008). The transducer, excited by a pulser/receiver (Model 5072PR) was connected to an oscilloscope (Model PC 5204) that converts analogue signal to digital. The sampling frequency of the pulser/receiver was 50MHz. The echoes from surface and subchondral junction reflections were recorded using PicoScope software (Pico Technology Limited, Cambridgeshire, UK). Speed of the sound in shoulder cartilage is reported to be 1780ms^{-1} (Graichen, 2003) and was taken for the thickness calculations. This value is larger than the typical values reported for bovine knee cartilage tissues, which is 1620-1680ms^{-1}. The difference is thought to be due to compositional difference between different joint cartilages, which is known to affect the speed of sound in cartilage tissues (Töyräs et al., 2003).

3.5 Mechanical indentation testing

Subchondral bone underneath the cartilage sample was properly constrained using a stainless steel holder (Fig. 1c), so as to ensure that the deformation data obtained was only due to the deformation of the cartilage. The indentation testing was carried out at 10^{-4}/s, 5×10^{-4}/s, 5×10^{-3}/s and 10^{-2}/s strain-rates (Fig. 1d). The samples were indented up to 30% engineering strain and a further limit of 3.5 MPa was imposed on the amount of stress that samples were subjected to, in order to minimize the potential damage to the tissues (Morel and Quinn, 2004; Quinn et al., 2001a). Also, before and every test, sample surfaces were microscopically examined (Leica MZ6, Leica microsystems, Heerbrugg, Switzerland) to check whether testing has induced any damage to the cartilage. The testing was done on a high resolution Instron testing machine (Model 5944, Instron, Canton, MA, USA) using a plane-ended, polished indenter of 3 mm diameter with 0.1mm radius rounded edge. The indenter with a rounded edge was used to reduce possible damage to the tissue due to stress concentration at the edge of the indenter. Depending on the thickness of samples, the speed of indentation was adjusted to obtain the required strain-rate. After each test, the cartilage was unloaded and allowed to recover for one hour in PBS-inhibitor solution prior to the next test. It has being experimentally demonstrated that the contact of the cartilage-solid indenter could well represent cartilage-cartilage contact experienced in joints (Oloyede and Broom, 1994). Additionally, the boundary condition between cartilage and solid indenter can be simulated readily by commercially available finite element software which has been used in the current study.

Figure 1 Here

----

4 Porohyperelastic Model

Cartilage was modeled as a porous, fluid saturated material, according to the poromechanics framework (See Appendix A.1 for details) (Biot, 1941; Simon, 1992). The model was developed in commercial finite element software (ABAQUS 6.12, Simulia, Rhode Island, USA). Axisymmetric elements were adopted to reduce the computational cost based on the characteristics of the test sample and loadings. The FE mesh

8

consisted of 7920 8-node bilinear displacement and bilinear pore pressure elements. The large deformations and geometric nonlinearity were considered in the model using non-linear strain definition. The 'pore-pressure (p)' (p=0) boundary condition was enforced on the upper surface of the portion, where the indenter does not touch the cartilage surface, and on the right side of the cartilage to enable fluid flow through these boundaries. The surface-to-surface contact between the cartilage and the indenter was modeled as the frictionless contact. The boundary condition of the impermeable boundary between rigid indenter and cartilage was set based on previous studies (Federico et al., 2008; Li et al., 1999). Given that the stiffness of both the indenter and the bone are several orders of magnitude higher than that of the cartilage, both of them were modeled as rigid bodies.

4.1 Solid skeleton material model

To account for the non-linear large deformation, the solid skeleton was modeled as an isotropic hyperelastic material. For isotropic hyperelastic materials, decoupled formulation with linear bulk modulus (K) small or of same order of magnitude to that of linear shear modulus (μ) would impose compressibility on the material (Ayyalasomayajula et al., 2010; Simon et al., 1998a). The current study uses the decoupled formulation by considering the cartilage as an isotropic material. However, it is important to mention that while it is relatively safe to use decoupled potential in the case of isotropy, in the case of anisotropy use of decoupled formulation would generally yield inaccurate results (Federico, 2010; Federico and Grillo, 2012).

The lower order material models, such as neo-Hookean or Mooney-Rivlin, cannot represent the highly nonlinear stress-strain behavior observed during this study (Supplementary materials: section S.1). Higher-order models such as the Yeoh model are considered more suitable in explaining the nonlinearity of cartilage tissues (Oloyede et al., 2009). However, the second-order reduced polynomial hyperelastic model gave an accurate description of the material behavior for the cartilage samples that were tested during the present study. Due to a few parameters in the second-order polynomial model, the Inverse FE analysis was used to obtain a unique set of material parameters. The form of second-order polynomial model used in this study is:

9

$$W^e = C_{10}(\bar{I}_1 - 3) + C_{20}(\bar{I}_1 - 3)^2 + \frac{1}{D_1}(J-1)^2 \tag{1}$$

Here, W^e is the (isotropic) elastic strain energy potential, $\bar{I}_1 = tr(\overline{C})$ is the first invariant of the distortional part $\overline{C} = \overline{F}^T \overline{F}$ of the right Cauchy deformation tensor $C = F^T F$ (where $\overline{F} = J^{-1/3} F$ is the distortional part of the deformation gradient F), and $J = \det F$ is the volume ratio. Furthermore, $\mu = 2C_{10}$, where μ is the shear modulus of linear elasticity, C_{20} is a nonlinear stiffness parameter, and $D_1 = 2/\kappa$, where κ is the bulk modulus of linear elasticity. The C_{20} is the coefficient of the nonlinear term $(\bar{I}_1 - 3)^2$ which determines the nonlinearity of stress-strain behavior.

4.2 Strain-dependent permeability and strain-rate-dependent permeability

The permeability (k) of cartilages decreases exponentially under application of strain and is given by Eq. (2) (Holmes and Mow, 1990; Lai and Mow, 1980; Wu and Herzog, 2000). In Eq. (2), e is the void ratio (ratio of volume of pores to volume of solid), a quantity representing 'dilatation', while e_0 is the initial void ratio. The parameter k_o is the permeability of the tissue in the undeformed configuration and M and m are dimensionless material parameters.

$$k = k_0 \left(\frac{e}{e_0} \right)^m exp \left\{ \frac{M}{2} \left[\left(\frac{1+e}{1+e_0} \right)^2 - 1 \right] \right\} \tag{2}$$

The permeability of cartilage is not only dependent on strain, but it is also a function of applied pressure difference (Lai and Mow, 1980). A higher-pressure difference would result in smaller permeability. This is can be due to the pressure-drag forces that are developed when the pressure difference is increased, which restricts the fluid movement. According to Oloyede and Broom (1992), as strain-rate increases, the pore-pressure inside the cartilage also increases. Therefore, an increase in the pressure difference between inside and outside of the tissue is expected with the increase in strain-rate. In addition, due to application of strain-

10

rate, there is a possibility that the inertial forces may also reduce fluid movement inside the tissue. Hence, overall permeability is expected to decrease with increase in strain-rate. A permeability function that considers the effect of strain-rate is not reported in literature. Nevertheless, we have re-analyzed the data of Lai and Mow (1980) and Oloyede and Broom (1992), and have introduced a mathematical relationship that represents permeability variation with strain and strain-rate (see supplementary materials: section S.2 for details). In addition to applied strain, the mathematical relationship illustrates that permeability decreases with the increase of the strain-rate [Fig. S3 (b)].

The decrease in permeability with strain-rate is reasonable given the mentioned evidences in permeability reduction with increase in applied pressure difference and inertial forces reducing the fluid movements. However, to authors' knowledge, there are no specific studies conducted to investigate to what extent the inertia forces affects fluid movement inside cartilage tissues at different strain-rates. It has been mentioned in Edelsten et al. (2010) that at high strain-rates (10/s to 10^3/s) , which occurs in less than 0.1s (Edelsten et al., 2010), inertia precludes significant water movement. The time scales of the experiments conducted in the present study is in the range of 30s (10^{-2}/s) to 3000s (10^{-4}/s). Therefore, the effect of inertia forces is arguably small at small strain-rates tested (10^{-4}/s) and might be starting to affect at highest strain-rate tested (10^{-2}/s). The mathematical relationship developed in the present study might have captured some aspects of the effect of inertia forces. However, since static permeability data was used to develop the relationship it might have not captured effect of fluid behavior under different strain-rates totally. The section 5.6, further mentions the assumptions made in developing mathematical relationship for permeability and the implications of the assumptions. Nevertheless, the obtained permeability function, i.e. the strain-rate-dependent permeability, was included in the porohyperelastic framework and the model predictions were compared with porohyperelastic models, which include strain-dependent permeability [Eq. (2)] and constant permeability. The parameters of Eq.(2), i.e. e_o , M and m were 4.0, 4.638 and 0.0848 respectively (Holmes and Mow, 1990). Throughout the rest of this manuscript, the porohyperelastic model with strain-dependent permeability and the porohyperelastic model with strain-rate-dependent permeability are named as the strain-dependent model and strain-rate-dependent model, respectively.

4.3 Material parameter identification

Material parameters of the second-order reduced polynomial model were extracted using the Inverse FE analysis. Following the approach developed by Simon et al. (1998b), considering the material as incompressible at the highest strain-rate (10^{-2}/s), C_{10} and C_{20} were obtained by fitting the force-indentation experimental data to the FE model prediction. The parameters D_1 and k_o were obtained by fitting the experimental data of force-indentation at the lowest strain-rate (10^{-4}/s) to the FE model prediction, considering the material as compressible. The obtained parameters were used to predict the strain-rate-dependent behavior of the cartilage tissues and were compared with the experimental results. Based on the performances of three porohyperelastic models—constant, strain-dependent, and strain-rate-dependent —the effect of solid-interstitial fluid interaction on strain-rate-dependent behavior was evaluated.

5 Results and Discussion

5.1 Mechanical behavior of kangaroo shoulder cartilage

The reported literature on the mechanical behavior kangaroo shoulder cartilages is limited. However, the experimental trends observed in the current investigation (Fig. 2) is consistent with the data reported for bovine patellar cartilages (DiSilvestro et al., 2001; Langelier and Buschmann, 2003; Li et al., 2003; Oloyede et al., 1992). Despite the tight control in sample selection and experimental set-up, a relatively large standard deviation was observed in the experimental data. This observation is not unusual, considering the reported experimental data on human shoulder cartilage (Huang et al., 2005). The large standard deviation is most likely to be due to inherent biological variation in samples. Throughout the paper, average data of samples with the corresponding positive standard deviation (SD) is provided in figures.

12

Figure 2 Here

As shown in Fig. 2, the stiffness of kangaroo shoulder cartilage increases with strain and strain-rate. The Repeated measures analysis of variance (ANOVA) test indicated that the increase in stiffness with strain and strain-rate is statistically significant at all levels (Turkey's pairwise comparisons, p<0.005). The stiffness reported by Langelier and Buschmann (2003) for bovine patella cartilages, under different strain-rates ($5x10^{-4}$/s, $5x10^{-3}$/s and $5x10^{-2}$/s) are higher than those in the current study (p<0.05). Nonetheless, the results are reasonable considering the fact that patellar cartilage bears high compressive loading compared to shoulder cartilage. Differences in species might have also contributed to the above differences in stiffness.

5.2 Biomechanical parameters of kangaroo shoulder cartilage

The second-order polynomial hyperelastic function fitted well to both high (R^2=0.9890 ± 0.0044, p<0.000) and low (R^2=0.9855 ± 0.0098, p<0.000) strain-rate data. The stiffness parameters, i.e. C_{10} and C_{20}, identified from the Inverse FE analysis, are 0.0988 ± 0.0622 MPa and 0.1482 ± 0.061 MPa, respectively. Similarly, the obtained compressibility parameter $1/D_1$, and the permeability in the undeformed configuration k_o are 0.0782 ± 0.055 MPa and 1.32 ± 0.98 x 10^{-14} m^4/Ns, respectively.

The hyperelastic material parameters for shoulder cartilage tissues are not reported elsewhere. Nevertheless, assuming Poisson's ratio (υ) to be 0.15 (Demarteau et al., 2006; Korhonen et al., 2002), Young's modulus (*E*) for kangaroo shoulder cartilage is 0.454 ± 0.286 MPa. The Young's modulus, *E*, calculated using

$$H_A = \frac{E(1-\upsilon)}{(1+\upsilon)(1-2\upsilon)}$$

for human shoulder cartilages, based on aggregate modulus (H_A), reported in Huang et al.'s (2005) and Mow et al.'s (1993) studies, is 0.214 MPa and 0.624 MPa respectively. The Young's modulus of kangaroo shoulder cartilage is not significantly different (p=0.109) from the Young's modulus of human shoulder cartilage obtained from Mow et al.'s (1993) study. But it is significantly different (p<0.05) from that

reported by Huang et al. (2005). Nevertheless, the average Young's modulus of kangaroo shoulder cartilages falls within the Young's modulus values reported for human shoulder cartilages.

The average thickness of kangaroo shoulder cartilage samples obtained through ultrasound measurements was 0.77 ± 0.10mm. The reported average thickness value for human shoulder cartilage is 1.44mm (Soslowsky et al., 1992), which is higher than that of kangaroo cartilages (p<0.005). Considering the differences in thickness and differences in tissue composition of different species, we would consider the average E value obtained in this study as acceptable. The permeability of kangaroo shoulder cartilage is relatively low, but is not significantly different (p=0.145) to that reported for the central region of human humeral head cartilage, which is $1.82 \pm 1.27 \times 10^{-14}$ m^4/Ns (Huang et al., 2005). The biomechanical properties and behavior of kangaroo shoulder cartilage are in general agreement with that of human shoulder cartilage tissues.

5.3 Comparison of constant, strain-dependent and strain-rate-dependent model predictions

----

Figure 3 Here

As shown in Fig 3, stresses predicted by the porohyperelastic FE models using constant, strain-dependent and strain-rate-dependent permeability, respectively, are compared with those obtained from experiments. In general, all models were sensitive to the strain-rate. However, the strain-rate-dependent and strain-dependent models were better than the model with constant permeability, at capturing the experimental results, at all strain-rates (Fig. 3d). Nevertheless, it should be noted that below 10% of strain all the model predictions were similar. At intermediate strain-rates, statistically significant differences (p<0.05) were identified between the model with constant permeability and the predictions of the other two models. This statistical difference was more significant when a similar comparison was made at the highest strain-rate (p<0.005) i.e., at 10^{-2}/s. Considering the R^2 values (Fig. 3d), the predictions of the strain-rate-dependent model were better than the strain-dependent model at all strain-rates. However, statistical differences were not identified

14

between the predictability of strain-dependent and strain-rate-dependent models at 5×10^{-3}/s (p=0.179), while at 5×10^{-4}/s model predictions were significantly different (p<0.05). Nevertheless, compared to the strain-dependent model (R^2=0.7937± 0.1478), the strain-rate-dependent model (R^2= 0.8915 ± 0.0662) was considerably better at predicting the stress-strain variation at the highest strain-rate at a higher significance level (p<0.005).

A stronger effect of permeability is expected if the flow field under the indenter is increased by using a bigger diameter indenter or unconfined, confined compression test. However, testing using porous indenter or platen, as mentioned by Buschmann et al. (1997), could lead to 400% error in the estimated permeability values using curve fitting the force-indentation curves to a FE model . Additionally, unless the porous filler is carefully characterized, it becomes difficult to define the boundary conditions accurately between the contacting surface and cartilage and also there is a possibility that repetitive loading can damage the tissue, especially under large deformations (Buschmann et al., 1997). The main reason for choosing indentation tests for the present study was, in vivo in joints, compression in cartilage is localised, and hence surrounding tissue is additionally subjected to tension, which is resembled by indentation tests. However, Indentation using a small indenter can be stated as a limitation of the present study. In order to observe a stronger effect of permeability, indentation using a bigger diameter indenter or unconfined compression testing can be conducted.

5.4 Effects of strain-dependent and strain-rate-dependent permeability

The strain-dependent permeability takes into account the shrinkage of pores during the deformation while the constant permeability does not consider the shrinkage of pores. Due to the reduction in pore size (i.e. reduction of effective flow area) with deformation, it becomes difficult for fluid to move out from the tissue. This reduction of the tissue's permeability leads to an increase in solid-interstitial fluid frictional-interactions. This must be the reason that both strain-dependent and strain-rate-dependent models outperformed the model with constant permeability at all strain-rates (p<0.05). When a strain is applied at a very short time interval, fluid will experience large pressure differences and also inertia will reduce fluid

15

movement significantly. Inertia force has been mentioned to significantly preclude the fluid movement when cartilage loaded at time scales less 0.1s (Edelsten et al., 2010). Therefore, effect of inertia on the fluid behavior can be considered to be small at small strain-rates, however might be starting to prevail at high strain-rates tested. Arguably, this could be the reason why the strain-rate-dependent model was better at capturing the experimental results at the highest strain-rate tested in the present study (p<0.005). Hence, in addition to the effect of strain on permeability, in order to better explain the tissue behavior at higher strain-rates, the effect of strain-rate on permeability can also be taken into account in future computational cartilage models.

Oloyede and Broom (1992), observed a dramatic increase in the effective stress of cartilage solid skeleton in comparison to pore-pressure increase when the strain-rate was increased from 10^{-3}/s to 10^{-2}/s. Fluid exudation from the cartilage decrease with increase in strain-rate and as observed in the results of the present study, at 10^{-2}/s model with strain-rate-dependent permeability was significantly better at capturing experimental results. Therefore, observation of Oloyede and Broom (1992) could be due to inertia forces beginning to affect the tissue behavior significantly , i.e. reduction of fluid movement at high strain-rates. This indicates that the effect of reduction of permeability with the strain-rate plays an important role at high strain-rates.

The fluid movement inside the cartilage is affected by the pore size of the tissue, which determines the permeability of the tissue. The typical pore size in cartilage is reported to be in the range of 20Å -65Å in its undeformed state (Linn and Sokoloff, 1965; Maroudas, 1973; Maroudas, 1975). Assuming cartilage is comprised of a network of pores, in the undeformed state, the pore size of the tissue in the current study, based on Eq. (3) (Maroudas, 1973) is 154.55 ± 46.1Å.

$$k_0 = \left(\frac{Hr^2}{\tau^2} \right) \left(\frac{1}{8\eta} \right) \tag{3}$$

Here, H is the volume fraction of the water (0.8), τ is the tortuosity of flow path (1.4), η is the fluid viscosity (10^{-3} Ns/m^2) and r is the pore size (Refer to Appendix A.2 for details). The pores, which are in scale of nanometres, will reduce further under deformation. The permeability reduction with strain and strain-rate helps to reduce excessive deformation of the tissue and would provide protection to the underlying bone at large strain-rates. In the case of osteoarthritis, where the proteoglycan content has been reported to be low, the pore size and permeability will be higher than a normal tissue (Korhonen et al., 2003). This will increase the possibility of excessive deformation in comparison to a healthy tissue, thus increasing the risk of bone-to-bone contact and tissue damage.

5.5 Mechanisms underlying the tissue behavior at large strain-rates

----

Figure 4 Here

Tension-compression nonlinearity (Park and Ateshian, 2006) and fluid pressure driven fibril stiffening (Li et al., 2003; Li and Herzog, 2004) are well-accepted mechanisms that facilitate cartilage to bear the load under dynamic loading and large strain-rates. In the present study, the strain-rate-dependent model shows higher pore-pressure at the highest strain-rate as compared with the strain-dependent model (Fig. 4a and 4b). The smaller fluid velocities observed (Fig. 4c) in the strain-rate-dependent model reflect reduction of permeability at high strain-rates. This confirms that at high strain-rates, strain-rate-dependent permeability

also enhances the fluid pressurization. This will also enable the tissue to respond to large strain-rates more effectively, such that excessive deformation of the tissue can be minimized.

5.6 Limitations of strain-rate-dependent permeability model

It is important to assess the limitation and assumptions under which the strain-rate-dependent permeability model of the present study has been formulated and possible implication of the assumptions. Currently there are no practical methods available to directly measure the fluid-flow rates inside cartilage tissue under different loading rates. The indirect method, as employed in the present study is to use fluid pressure measurements inside the tissue under different strain-rates and related them to available static permeability measurements under different pressures gradients. In static permeability measurement, a pressure gradient is imposed on already compressed cartilage and amount of fluid outflow is measured at equilibrium. When the tissue is compressed at a certain loading rate the fluid pressure in the loaded area will increase and there will be pressure gradient between loaded area and outside which is happening at a time scale smaller than that of static measurements. Additionally, during compression, fluid pressure in the loaded area continuously changes and is non-uniform. Therefore, static permeability measurements extracted at difference pressure gradients does not represent the actual conditions ideally and hence may affect the permeability values predicted by the strain-rate-dependent permeability model. The extents to which assumptions affect the strain-rate-dependent permeability model predictions require more investigations.

5.7 Possible improvements to porohyperelastic model with strain-rate-dependent permeability

The strain-rate-dependent model did not fit well to the stress-strain response at the highest strain-rate (10^{-2}/s) and some low strain-rates such as 5×10^{-4}/s. Although the main focus of the present study was not to present a comprehensive FE model to predict the experimental data, this can be stated as one of the limitations of the strain-rate-dependent model. Earlier studies have shown that fluid pressurization is enhanced by anisotropy of the elastic properties of the tissue (Huang et al., 2001; Huang and Gu, 2007). Furthermore, the anisotropy of cartilage permeability due to the glycosaminoglycan network deformation (Ateshian and Weiss, 2010; Quinn et al., 2001b; Reynaud and Quinn, 2006) and the collagen fibre orientation (Federico and Grillo,

18

2012; Federico and Herzog, 2008a; Federico and Herzog, 2008b; Pierce et al., 2013a; Pierce et al., 2013b; Tomic et al., 2014) affects the fluid pressurization at both small and large strains. Additionally, as mentioned earlier, there is evidence that flow-independent viscoelasticity of the cartilage matrix affects the strain-rate-dependent behavior of the tissue at small and large strain-rates (DiSilvestro et al., 2001; Edelsten et al., 2010; Huang et al., 2001). Hence, lower stresses predicted by the strain-rate-dependent model at low strain-rates, for example at 5×10^{-4}/s, might be improved by inclusion of matrix viscoelasticity in to the model. Also, we believe that by taking into account the anisotropic nature of the tissue and the effect of the viscoelasticity, the model prediction at highest strain-rate can also be improved. Therefore, inclusion of tissue anisotropy and viscoelasticity of cartilage matrix would be the next step to improve the quality of model prediction.

6 Conclusion and Remarks

In this paper, comprehensive indentation experiments were conducted on kangaroo shoulder cartilage tissues under different strain-rates. A porohyperelastic model was then developed based on the experimental characterizations. By introducing the strain-rate-dependent permeability into the porohyperelastic model and comparing the model predictions using constant and strain-dependent models, the present study has explained how the solid-interstitial fluid interaction facilitates the strain-rate-dependent behavior of shoulder cartilage tissues and its physiological relevance.

It was found that the strain-rate-dependent model can better capture the experimental results compared to strain-dependent model. Additionally, at the highest strain-rate, a statistically significant difference was found between strain-dependent and strain-rate-dependent model predictions. Therefore, it can be claimed that rate-dependent fluid behavior plays an important role in tissue deformation behavior at high strain-rates. With regards to an observation from an earlier study, where a transition of tissue behavior was observed at 10^{-2}/s (Oloyede and Broom, 1992), we state that this phenomenon is due to the reduction of pore size with strain and inertia forces beginning to affect the tissue behavior. The reduction of permeability with strain and strain-rate helps to reduce excessive deformation. This assists the tissues to function as a protective

layer for bone-ends during injurious loads at high strain-rates. Based on the findings of this study, FE models will benefit from the inclusion of strain-rate-dependent permeability to better predict the cartilage tissue response, especially at large strain-rates.

In addition to the above-mentioned conclusions, the study also concludes that kangaroo can be considered as a potential animal model for future research on shoulder cartilage. This is because the biomechanical properties of kangaroo cartilages were in general agreement with that of human shoulder cartilage tissues. Apart from that, considering the different loading encountered in the kangaroo's upper and lower-limb cartilages, it provides a natural source to investigate how mechanical forces affect the development, composition (e.g. proteoglycan distribution), structure (e.g. collagen architecture) of cartilage, and the progression of osteoarthritis. Further, experimentation on this animal model may also have the potential to give insights into how tissue-engineering strategies must be adjusted to develop joint specific tissues.

Acknowledgement

Appendices

A.1 Porohyperelastic field theory for soft biological tissues

The governing equations of porohyperelastic theory can be found in Simon (1992), Kaufmann (1996) and Ayyalasomayajula et al.(2010), and are summarized below. Porohyperelastic theory assumes that biological tissues can be represented as porous incompressible solid skeleton (*s*) statured with an incompressible fluid (*f*). The solid skeleton is hyperelastic in nature. The fluid is free to move relative to the solid depending on the solid deformation behavior and friction (Kaufmann, 1996). Further, the pores are assumed to be small. Therefore, the material can be viewed as a continuum. The ABAQUS (Abaqus 6.12, Simulia, Rhode Island, USA) commercial software along with the strain-rate-dependent permeability function introduced in the current study was used to model the cartilage tissue based on the porohyperelastic field theory.

According to the porohyperelastic field theory,

$$dV = dV^s + dV^f \tag{A.1}$$

Where V is the volume of individual solid and fluid components. The porosity (n) and the void ratio (e) is defined as

$$n = \frac{dV^f}{dV} = 1 - J^{-1}(1 - n_0) ; n_0 \text{ is the initial porosity} \tag{A.2}$$

$$e = \frac{dV^f}{dV^s} = \frac{n}{1-n} \tag{A.3}$$

The deformation gradient ($\mathbf{F}$) and the volume ratio (J) is given by

$$F_{iI} = \frac{\partial \chi_i}{\partial X_I} \tag{A.4}$$

$$J = \det(\mathbf{F}) \tag{A.5}$$

Where χ is the configuration map, which maps, at each time t, points $X = (X_1, X_2, X_3)$ in the reference configuration into a point $x = (x_1, x_2, x_3)$ in space, i.e., $x = \chi(X, t)$.

Governing equations, when expressed using Lagrangian description, are as follows.

- *Conservation of linear momentum*

$$\frac{\partial T_{iI}}{\partial X_I} = 0 \quad (T_{iI} \neq T_{Ii}) \tag{A.6}$$

21

Here, $\mathbf{T}$ is the first Piola-Kirchoff stress.

- *Conservation of fluid mass (Darcy's law)*

$$\tilde{v}_i^{fs} = -k_{ij}\left(\frac{d\pi^f}{dx_j}\right); \quad k_{ij} = k_0 f(e) \tag{A.7}$$

Where the velocity of the fluid is relative to the solid $\mathbf{v}^{fs} = \mathbf{v}^f - \mathbf{v}^s$ and the filtration velocity $\tilde{\mathbf{v}}^{fs} = n(\mathbf{v}^f - \mathbf{v}^s)$. In equation A.7, π^f and k are excess pore fluid pressure and hydraulic permeability respectively. Further, permeability is a function of deformation and hence, depends on the void ratio. The parameter k_0 is the tissue permeability at undeformed state.

- *Conservation of total mass*

Neglecting the inertial terms, the equation of balance of mass

$$div[(1-n)\mathbf{v}^s + n\mathbf{v}^f] = 0 \tag{A.8}$$

Hence,

$$div(\mathbf{v}^s) + div[n(\mathbf{v}^f - \mathbf{v}^s)] = 0 \tag{A.9}$$

Using the definition of filtration velocity

$$div(\mathbf{v}^s) + div(\tilde{\mathbf{v}}^{fs}) = 0 \tag{A.10}$$

- *Effective stress principle*

$$\sigma_{ij}^{total} = \sigma_{ij}^{eff} - \pi^f \delta_{ij}; \; \delta_{ij} = \begin{cases} 1 & i = j \\ 0 & i \neq j \end{cases} \tag{A.11}$$

$$S_{IJ}^{total} = S_{IJ}^{eff} - J\pi^f H_{IJ} \tag{A.12}$$

where σ_{ij}^{total}, σ_{ij}^{eff} are total Cauchy stress and effective stress of the solid skeleton, respectively. The corresponding components of second Piola-Kirchhoff stress are S_{IJ}^{total} and S_{IJ}^{eff}. Here, $\mathbf{H}$ is Finger's strain which is given by $H_{IJ} = F_{Ik}^{-1} F_{Jk}^{-1}$. The σ_{ij}^{eff} is calculated from the drained effective strain energy density function (W^e) as follows.

$$\sigma_{ij}^{eff} = J^{-1} F_{iI} S_{IJ}^{eff} F_{Jj}^T, \; S_{IJ}^{eff} = JF_{Ii}^{-1} \sigma_{ij} F_{jJ}^{-T} \tag{A.13}$$

$$S_{IJ}^{eff} = 2\frac{\partial W^e}{\partial C_{IJ}} = \frac{\partial W^e}{\partial E_{IJ}} \tag{A.14}$$

22

The Green strain tensor $E = \frac{1}{2}(C - I)$ and $C = F^T F$ is the right Cauchy-Green deformation tensor.

- Drained effective strain energy for Isotropic material can be written as

$$W^e = W^e(\bar{I}_1, \bar{I}_2, J) \hspace{3cm} \text{A.15}$$

Where $\bar{I}_1 = J^{-2/3} I_1$, $\bar{I}_2 = J^{-2/3} I_2$ and $I_1 = tr(C)$, $I_2(C) = \frac{1}{2}[(tr(C))^2 - tr(C^2)]$. For our study, as mentioned in the manuscript, the solid skeleton effective strain energy is represented by a second order reduced polynomial hyperelastic potential.

A.2 Pore size calculation based on permeability

The details of the Eq. (3), used in this manuscript to calculate the pore size, is summarized below based on the text of Maroudas (1973). Here, cartilage is considered as a porous material, comprising of a network of pores with an average pore radius (r) and tortuosity (τ). The path of the fluid movement in a porous structure is likely to be tortuous. Take L_e as the actual flow length and L as the 'darcian' flow length. Then the true pressure gradient, accounting for tortuosity can be written as,

$$\frac{dP}{dL} = \left(\frac{L_e}{L}\right)\frac{dP}{dL_e} \text{, here } P \text{ is the pressure} \hspace{2cm} \text{A.16}$$

Applying poiseuille equation to pore capillaries, the velocity of flow (v_f)

$$v_f = -\left(\frac{r^2}{8\eta}\right)\frac{dP}{dL_e} = -\left(\frac{r^2}{8\eta}\right)\frac{dP}{dL}\frac{L}{L_e} \hspace{2cm} \text{A.17}$$

Where η is the viscosity of the fluid. Then velocity of the flow is related to the fluid flux (q) and porosity or the volume fraction of water (H) by

$$v_f = \frac{q}{H}\frac{L_e}{L} \hspace{3cm} \text{A.18}$$

Substituting Eq. (A.17) to Eq. (A.18), the fluid flux is

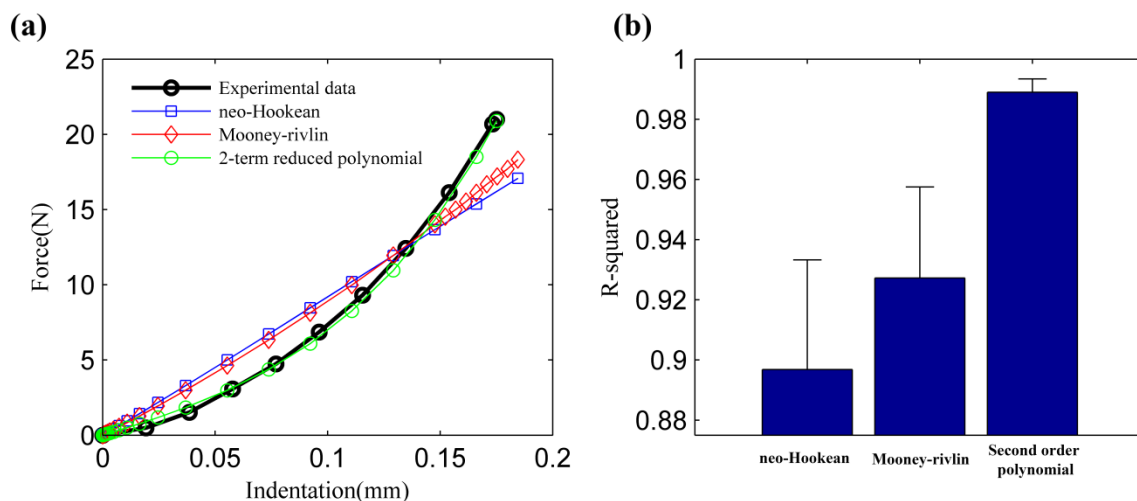$$q = -\frac{Hr^2}{8\eta}\left(\frac{L}{L_e}\right)^2\frac{dP}{dL} \qquad\qquad \text{A.19}$$

Comparing Eq. (A.19) with Darcy's law, the following Eq. (A.20) for the permeability can be obtained.

$$k = \left(\frac{Hr^2}{\tau^2}\right)\frac{1}{8\eta} \ ; \ \tau = \frac{L_e}{L} \qquad\qquad \text{A.20}$$

24

Supplementary Materials

S.1 Comparison of neo-Hookean, Mooney-rivlin and Second-order reduced polynomial hyperelastic model

Fig. S1 (a) Experimental data from 10^{-2}/s of a representative samples fitted to neo-Hookean, Mooney-Rivlin and 2-term reduced polynomial incompressible hyperelastic functions **(b)** The R-squared values indicating the goodness of fit of neo-Hookean, Mooney-Rivlin and second-order reduced polynomial hyperelastic functions to experimental data (n=10).

S.2 Strain-rate-dependent permeability function

In the following supplementary materials, the steps of obtaining a mathematical relationship for the permeability in terms of strain and strain-rate are mentioned. The data of Lai and Mow (1980), and Oloyede and Broom (1992), were used to obtain the relationship along with some approximations, which are mentioned in the text below.

Mow and Lai (1979) experimentally found that permeability is a function of strain and applied pressure difference (P). An exponential relationship between permeability and strain has been reported for infinitesimal strain (Lai and Mow, 1980). This equation has been further extended for large strain (Holmes and Mow, 1990; Wu and Herzog, 2000). Based on the above formulations, in the current study we have further shown the effect of strain-rate on permeability.
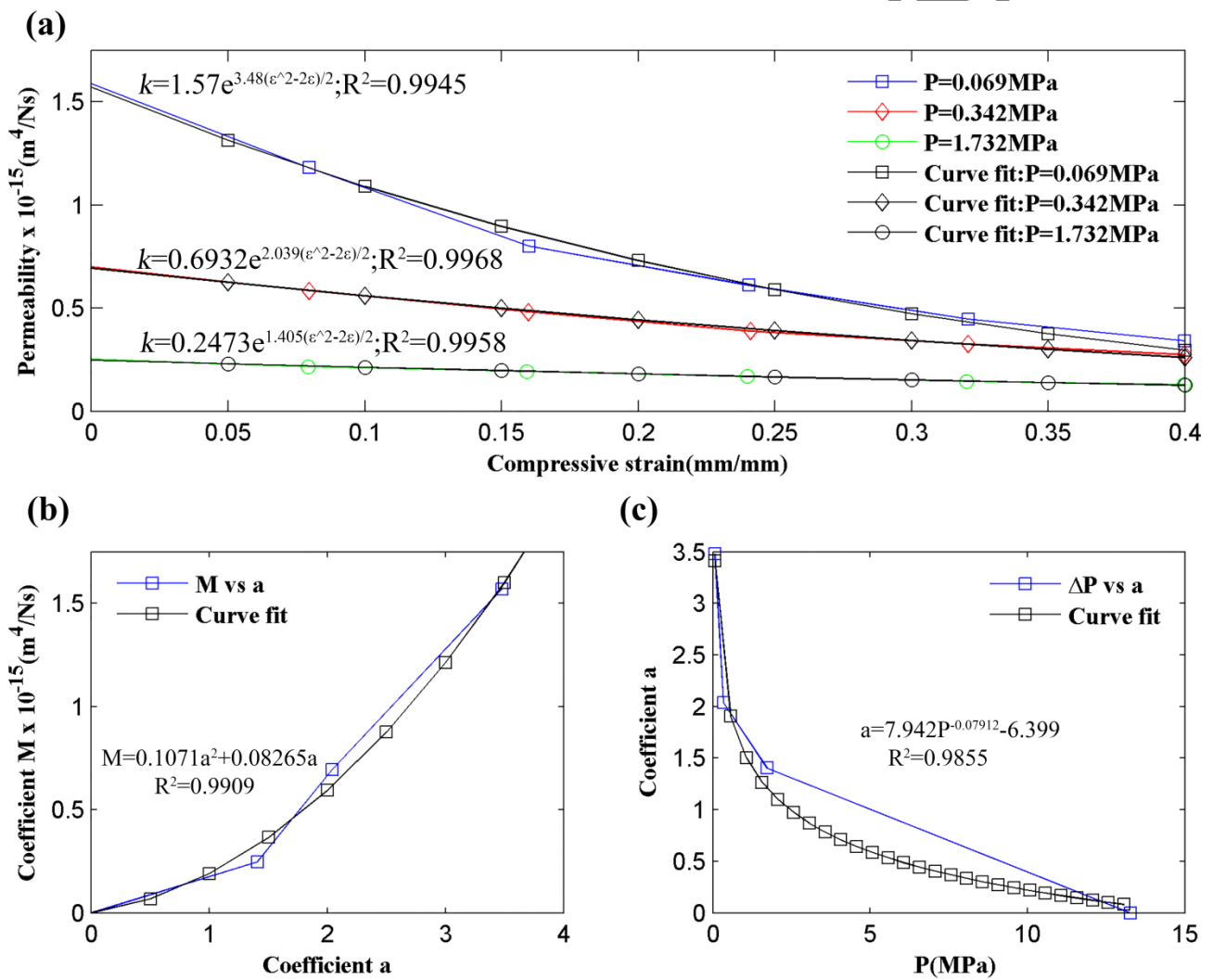
The isotropic permeability tensor ($\mathbf{k}$) can expressed as

$$\mathbf{k} = k\mathbf{I}$$

The scalar valued permeability function k can be represented by the following equation, where permeability is an exponential function of J, the volume ratio (Ateshian and Weiss, 2010; Holmes and Mow, 1990).

$$k = M \exp\left(a(J^2 - 1)/2\right) \qquad\qquad \text{S.1}$$

Fig. S2 (a) An exponential function (Eq. S.1) fitted to Lai and Mow (1980) data **(b)** Variation of coefficient M with coefficient a is approximated as a second order polynomial function **(c)** Variation of coefficient a with pressure difference (P) approximated as a power function

The data of Mow and Lai (1979), from one-dimensional permeation experiments, can be fitted to Eq. (S.1) for each pressure difference (P) [Fig. S2 (a)] to obtain the corresponding a and M values, which depend on applied strain and pressure difference. Considering the trend in permeability decrease with applied pressure difference, it is expected that at a certain high value of P permeability will reduce almost to zero. Therefore, at this pressure value, a and M will be almost zero. The resulting variation of a vs. M [Fig. S2 (b)] can be approximated as a second order polynomial function of the form of Eq. (S.2), where α and β are empirical constants.

$$M = \alpha a + \beta a^2 \qquad\qquad \text{S.2}$$

The P value at which coefficient a becomes almost zero is not available in the literature. Therefore, we assumed this P to be a high physiological joint contact pressure (e.g. contact pressure during high-speed running). Contact pressure inside the knee during high-speed running (5-10.5 m/s) is approximately 3.5 (Weyand et al., 2009; Weyand et al., 2010) times the static contact pressure. This is assuming that the ground reaction forces are proportional to the joint contact pressures. The reported static mean contact pressure values in knees are 2.75-3.79 MPa (Ahmed and Burke, 1983; Donahue et al., 2002; Huang et al., 2002). Therefore, P at which a becomes zero was taken to be 13.625 MPa.

The variation of P vs. a was approximated by a power relationship [Eq. (S.3) and Fig. S2(c)], where γ, δ and λ are empirical constants. In this derivation, we have used simple functional forms that can represent the relationship between different variables. Some may prefer to use other functional forms, which are equally correct.

$$a = \gamma P^{\delta} + \lambda \qquad\qquad \text{S.3}$$

After re-analyzing the data of Oloyede and Broom (1992), it can be seen that the internal pore-pressure of a cartilage increases—under compression—with increasing strain and strain-rate [Fig. S3(a)]. This increase in pore-pressure values will result in increased pressure differences between inside and outside of the tissue.

Assuming that the internal pore-pressure is proportional to P, an approximate relationship between P, strain-rate and strain can be obtained [Eq. (S.4)]. Here in Eq. (S.4) ϕ is an empirical constant.

$$P = \phi(J-1)D^{1/2} \qquad\qquad \text{S.4}$$

Here D is the rate of deformation. The deformation rate tensor, $\mathbf{D} = grad(\mathbf{v})$ (i.e. $D_{ij} = \partial \upsilon_i / \partial x_j$).
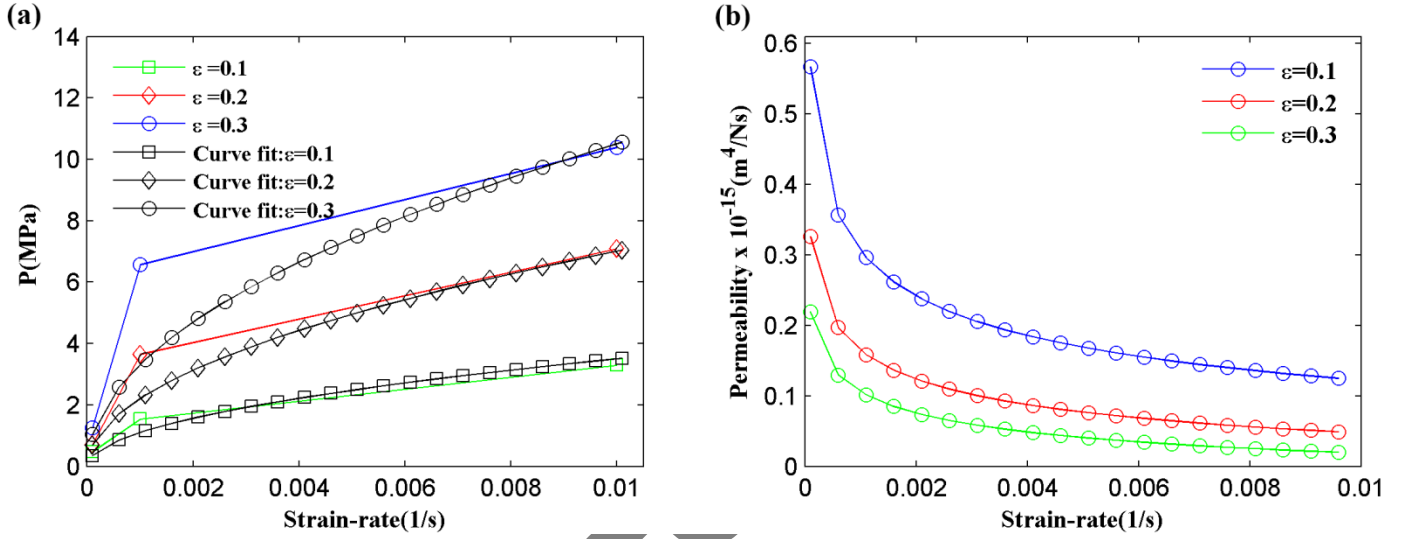
Fig. S3 (a) Data of Oloyede and Broom (1992) re-analyzed: Variation of pressure difference (P) between inside and outside of the tissue with strain-rate **(b)** Variation of permeability with strain-rate as predicted by Eq. (S.5)

Combining Eq. (S.1) and Eq. (S.4), a mathematical relationship can be obtained for permeability [Eq. (S.5)], where it is a function of strain and strain-rate:

$$k = a(\alpha + \beta a)\exp\left(a(J^2-1)/2\right) \text{ Where } a = \gamma P^\delta + \lambda \qquad\qquad \text{S.5}$$

The values of the empirical parameters obtained using the data of Lai and Mow (1980) and Oloyede and Broom (1992) are as follows: α =0.0827, β =0.1071, ϕ =350.27, λ=-6.399, γ =7.942, and δ =-0.0791. Based on the obtained parameters we have predicted the variation of permeability in terms of strain and strain-rate as shown in Fig. S3 (b). The permeability was found to be decreasing with both strain and strain-rate.

References

Ahmed, A., Burke, D., 1983. In-Vitro of Measurement of Static Pressure Distribution in Synovial Joints—Part I: Tibial Surface of the Knee. Journal of biomechanical engineering 105, 216-225.

Ateshian, G.A., Weiss, J.A., 2010. Anisotropic hydraulic permeability under finite deformation. Journal of Biomechanical Engineering 132, 111004.

Ayyalasomayajula, A., Vande Geest, J.P., Simon, B.R., 2010. Porohyperelastic finite element modeling of abdominal aortic aneurysms. J Biomech Eng 132, 104502.

Bingham, J., Papannagari, R., Van de Velde, S., Gross, C., Gill, T., Felson, D., Rubash, H., Li, G., 2008. In vivo cartilage contact deformation in the healthy human tibiofemoral joint. Rheumatology 47, 1622-1627.

Biot, M.A., 1941. General theory of three‐dimensional consolidation. Journal of applied physics 12, 155-164.

Brown, C., Hughes, S., Crawford, R., Oloyede, A., 2008. Joint laminate degradation assessed by reflected ultrasound from the cartilage surface and osteochondral junction. Phys Med Biol 53, 4123.

Buschmann, M.D., Soulhat, J., Shirazi-Adl, A., Jurvelin, J.S., Hunziker, E.B., 1997. Confined compression of articular cartilage: linearity in ramp and sinusoidal tests and the importance of interdigitation and incomplete confinement. J Biomech 31, 171-178.

Changoor, A., Fereydoonzad, L., Yaroshinsky, A., Buschmann, M.D., 2010. Effects of refrigeration and freezing on the electromechanical and biomechanical properties of articular cartilage. J Biomech Eng 132, 064502.

Demarteau, O., Pillet, L., Inaebnit, A., Borens, O., Quinn, T.M., 2006. Biomechanical characterization and in vitro mechanical injury of elderly human femoral head cartilage: comparison to adult bovine humeral head cartilage. Osteoarthritis Cartilage 14, 589-596.

DiSilvestro, M.R., Zhu, Q., Suh, J.-K.F., 2001. Biphasic Poroviscoelastic Simulation of the Unconfined Compression of Articular Cartilage: II—Effect of Variable Strain Rates. Journal of Biomechanical Engineering 123, 198.

Donahue, T.L.H., Hull, M., Rashid, M.M., Jacobs, C.R., 2002. A finite element model of the human knee joint for the study of tibio-femoral contact. Journal of biomechanical engineering 124, 273-280.

Edelsten, L., Jeffrey, J.E., Burgin, L.V., Aspden, R.M., 2010. Viscoelastic deformation of articular cartilage during impact loading. Soft Matter 6, 5206-5212.

Farkas, T., Boyd, R., Schaffler, M., Radin, E., Burr, D., 1987. Early vascular changes in rabbit subchondral bone after repetitive impulsive loading. Clinical orthopaedics and related research, 259.

Federico, S., 2010. Volumetric-distortional decomposition of deformation and elasticity tensor. Mathematics and Mechanics of Solids.

Federico, S., Grillo, A., 2012. Elasticity and permeability of porous fibre-reinforced materials under large deformations. Mechanics of Materials 44, 58-71.

Federico, S., Grillo, A., Imatani, S., Giaquinta, G., Herzog, W., 2008. An energetic approach to the analysis of anisotropic hyperelastic materials. International Journal of Engineering Science 46, 164-181.

Federico, S., Herzog, W., 2008a. On the anisotropy and inhomogeneity of permeability in articular cartilage. Biomech Model Mechanobiol 7, 367-378.

Federico, S., Herzog, W., 2008b. On the permeability of fibre-reinforced porous materials. International Journal of Solids and Structures 45, 2160-2172.

Finlay, J., Repo, R., 1979. Energy absorbing ability of articular cartilage during impact. Medical and Biological Engineering and Computing 17, 397-403.

Graichen, H., 2003. Validation of cartilage volume and thickness measurements in the human shoulder with quantitative magnetic resonance imaging. Osteoarthritis and Cartilage 11, 475-482.

He, B., Wu, J., Chim, S., Xu, J., Kirk, T., 2013. Microstructural analysis of collagen and elastin fibres in the kangaroo articular cartilage reveals a structural divergence depending on its local mechanical environment. Osteoarthritis and Cartilage 21, 237-245.

Holmes, M., Mow, V., 1990. The nonlinear characteristics of soft gels and hydrated connective tissues in ultrafiltration. J Biomech 23, 1145-1156.

Huang, A., Hull, M., Howell, S.M., Donahue, T.H., 2002. Identification of cross-sectional parameters of lateral meniscal allografts that predict tibial contact pressure in human cadaveric knees. Journal of biomechanical engineering 124, 481-489.

Huang, C.-Y., Mow, V.C., Ateshian, G.A., 2001. The Role of Flow-Independent Viscoelasticity in the Biphasic Tensile and Compressive Responses of Articular Cartilage. Journal of Biomechanical Engineering 123, 410.

Huang, C.Y., Gu, W.Y., 2007. Effects of tension-compression nonlinearity on solute transport in charged hydrated fibrous tissues under dynamic unconfined compression. Journal of Biomechanical Engineering 129, 423-429.

Huang, C.Y., Stankiewicz, A., Ateshian, G.A., Mow, V.C., 2005. Anisotropy, inhomogeneity, and tension-compression nonlinearity of human glenohumeral cartilage in finite deformation. J Biomech 38, 799-809.

Julkunen, P., Wilson, W., Isaksson, H., Jurvelin, J.S., Herzog, W., Korhonen, R.K., 2013. A review of the combination of experimental measurements and fibril-reinforced modeling for investigation of articular cartilage and chondrocyte response to loading. Computational and mathematical methods in medicine 2013, 326150.

Kaufmann, M.V., 1996. Porohyperelastic analysis of large arteries including species transport and swelling effects. University of Arizona.

Korhonen, R., Laasanen, M., Töyräs, J., Rieppo, J., Hirvonen, J., Helminen, H., Jurvelin, J., 2002. Comparison of the equilibrium response of articular cartilage in unconfined compression, confined compression and indentation. J Biomech 35, 903-909.

Korhonen, R.K., Laasanen, M.S., Töyräs, J., Lappalainen, R., Helminen, H.J., Jurvelin, J.S., 2003. Fibril reinforced poroelastic model predicts specifically mechanical behavior of normal, proteoglycan depleted and collagen degraded articular cartilage. J Biomech 36, 1373-1379.

Lai, W., Mow, V., 1980. Drag-induced compression of articular cartilage during a permeation experiment. Biorheology 17, 111.

Lai, W., Mow, V.C., Roth, V., 1981. Effects of nonlinear strain-dependent permeability and rate of compression on the stress behavior of articular cartilage. Journal of biomechanical engineering 103, 61-66.

Langelier, E., Buschmann, M.D., 2003. Increasing strain and strain rate strengthen transient stiffness but weaken the response to subsequent compression for articular cartilage in unconfined compression. J Biomech 36, 853-859.

Li, L., Soulhat, J., Buschmann, M., Shirazi-Adl, A., 1999. Nonlinear analysis of cartilage in unconfined ramp compression using a fibril reinforced poroelastic model. Clin Biomech (Bristol, Avon) 14, 673-682.

Li, L.P., Buschmann, M.D., Shirazi-Adl, A., 2003. Strain-rate Dependent Stiffness of Articular Cartilage in Unconfined Compression. Journal of Biomechanical Engineering 125, 161.

Li, L.P., Herzog, W., 2004. Strain-rate dependence of cartilage stiffness in unconfined compression: the role of fibril reinforcement versus tissue volume change in fluid pressurization. J Biomech 37, 375-382.

Linn, F.C., Sokoloff, L., 1965. Movement and composition of interstitial fluid of cartilage. Arthritis & Rheumatism 8, 481-494.

Liu, F., Kozanek, M., Hosseini, A., Van de Velde, S.K., Gill, T.J., Rubash, H.E., Li, G., 2010. In vivo tibiofemoral cartilage deformation during the stance phase of gait. J Biomech 43, 658-665.

Longo, U.G., Forriol, F., Campi, S., Maffulli, N., Denaro, V., 2011. Animal models for translational research on shoulder pathologies: from bench to bedside. Sports Med Arthrosc 19, 184-193.

Maroudas, A., 1973. Physico-chemical Properties of Articular Cartilage, in: Freeman, M. (Ed.), Adult Articular Cartilage. Pitman Medical, London, pp. pp. 131–170.

Maroudas, A., 1975. Biophysical chemistry of cartilaginous tissues with special reference to solute and fluid transport. Biorheology 12, 233.

Morel, V., Quinn, T.M., 2004. Cartilage injury by ramp compression near the gel diffusion rate. Journal of orthopaedic research 22, 145-151.

Mow, V., Bigliani, L., Flatow, E., Ticker, J., Ratcliffe, A., Soslowsky, L., 1993. Material properties of the inferior glenohumeral ligament and the glenohumeral articular cartilage. The Shoulder: a balance of mobility and stability. Rosemont, IL, AAOS, 29-68.

Mow, V.C., Lai, W., 1979. Mechanics of animal joints. Annual review of Fluid mechanics 11, 247-288.

Oloyede, A., Broom, N., 1992. Stress-sharing between the fluid and solid components of articular cartilage under varying rates of compression. Connective tissue research 30, 127-141.

Oloyede, A., Broom, N.D., 1994. The generalized consolidation of articular cartilage: an investigation of its near-physiological response to static load. Connective tissue research 31, 75-86.

Oloyede, A., Crawford, R.W., Moody, H.R., Nguyen, T.C., Brown, C.P., 2009. Assessment of common hyperelastic constitutive equations for describing normal and osteoarthritic articular cartilage. Proceedings of the Institution of Mechanical Engineers, Part H: Journal of Engineering in Medicine 223, 643-652.

Oloyede, A., Flachsmann, R., Broom, N.D., 1992. The dramatic influence of loading velocity on the compressive response of articular cartilage. Connective tissue research 27, 211-224.

Park, S., Ateshian, G.A., 2006. Dynamic response of immature bovine articular cartilage in tension and compression, and nonlinear viscoelastic modeling of the tensile response. Journal of Biomechanical Engineering 128, 623-630.

Pierce, D., Ricken, T., Holzapfel, G.A., 2013a. Modeling sample/patient‐specific structural and diffusional responses of cartilage using DT‐MRI. International journal for numerical methods in biomedical engineering 29, 807-821.

Pierce, D.M., Ricken, T., Holzapfel, G.A., 2013b. A hyperelastic biphasic fibre-reinforced model of articular cartilage considering distributed collagen fibre orientations: continuum basis, computational aspects and applications. Comput Methods Biomech Biomed Engin 16, 1344-1361.

Qu, C., Hirviniemi, M., Tiitu, V., Jurvelin, J.S., Toyras, J., Lammi, M.J., 2013. Effects of Freeze-Thaw Cycle with and without Proteolysis Inhibitors and Cryopreservant on the Biochemical and Biomechanical Properties of Articular Cartilage. Cartilage 5, 97-106.

Quinn, T., Allen, R., Schalet, B., Perumbuli, P., Hunziker, E., 2001a. Matrix and cell injury due to sub‐impact loading of adult bovine articular cartilage explants: effects of strain rate and peak stress. Journal of orthopaedic research 19, 242-249.

Quinn, T., Dierickx, P., Grodzinsky, A., 2001b. Glycosaminoglycan network geometry may contribute to anisotropic hydraulic permeability in cartilage under compression. J Biomech 34, 1483-1490.

Radin, E.L., Paul, I.L., LowY, M., 1970. A comparison of the dynamic force transmitting properties of subchondral bone and articular cartilage. The Journal of Bone & Joint Surgery 52, 444-456.

Reynaud, B., Quinn, T.M., 2006. Tensorial electrokinetics in articular cartilage. Biophys J 91, 2349-2355.

Rubin, C.T., Lanyon, L.E., 1982. Limb mechanics as a function of speed and gait: a study of functional strains in the radius and tibia of horse and dog. Journal of experimental biology 101, 187-211.

Simon, B., Kaufmann, M., McAfee, M., Baldwin, A., 1998a. Porohyperelastic finite element analysis of large arteries using ABAQUS. Journal of biomechanical engineering 120, 296.

Simon, B., Kaufmann, M., McAfee, M., Baldwin, A., Wilson, L., 1998b. Identification and determination of material properties for porohyperelastic analysis of large arteries. Journal of biomechanical engineering 120, 188-194.

Simon, B.R., 1992. Multiphase poroelastic finite element models for soft tissue structure. Applied Mechanics Reviews 45.

Soltz, M.A., Ateshian, G.A., 2000. Interstitial fluid pressurization during confined compression cyclical loading of articular cartilage. Annals of biomedical engineering 28, 150-159.

Sonnabend, D., Young, A., 2009. Comparative anatomy of the rotator cuff. Journal of Bone & Joint Surgery, British Volume 91, 1632-1637.

Soslowsky, L.J., Flatow, E.L., Bigliani, L.U., Mow, V.C., 1992. Articular geometry of the glenohumeral joint. Clinical Orthopaedics and Related Research 285, 181-190.

Thompson, R.C., Vener, M., Griffiths, H., Lewis, J., Oegema, T., Wallace, L., 1993. Scanning electron-microscopic and magnetic resonance-imaging studies of injuries to the patellofemoral joint after acute transarticular loading. The Journal of Bone & Joint Surgery 75, 704-713.

Tomic, A., Grillo, A., Federico, S., 2014. Poroelastic materials reinforced by statistically oriented fibres--numerical implementation and application to articular cartilage. IMA Journal of Applied Mathematics 79, 1027-1059.

Töyräs, J., Laasanen, M.S., Saarakkala, S., Lammi, M.J., Rieppo, J., Kurkijärvi, J., Lappalainen, R., Jurvelin, J.S., 2003. Speed of sound in normal and degenerated bovine articular cartilage. Ultrasound Med Biol 29, 447-454.

Weyand, P.G., Bundle, M.W., McGowan, C.P., Grabowski, A., Brown, M.B., Kram, R., Herr, H., 2009. The fastest runner on artificial legs: different limbs, similar function? J Appl Physiol (1985) 107, 903-911.

Weyand, P.G., Sandell, R.F., Prime, D.N., Bundle, M.W., 2010. The biological limits to running speed are imposed from the ground up. J Appl Physiol (1985) 108, 950-961.

Wu, J., Herzog, W., 2000. Finite element simulation of location-and time-dependent mechanical behavior of chondrocytes in unconfined compression tests. Annals of Biomedical Engineering 28, 318-330.

33

Figure. S3   (a) Data of Oloyede and Broom (1992) re-analyzed: Variation of pressure difference (P) between inside and outside of the tissue with strain-rate (b) Variation of permeability with strain-rate as predicted by Eq. (S.5)

Figures

Fig. 1 (a) A 8mm diameter cartilage sample **(b)** Specimen harvested region: Near the central area of humeral head **(c)** Bone was constrained using a stainless steel holder and submerged in physiological (0.15M) saline solution **(d)** Indentation testing on the sample.
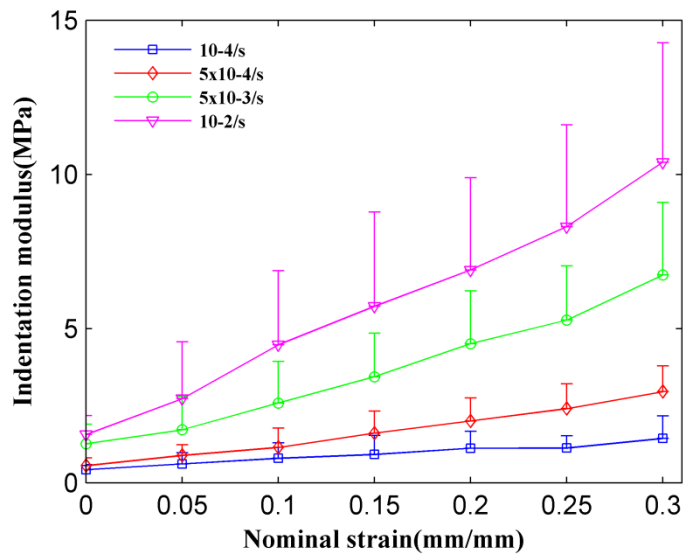
Fig. 2 Stiffness variation with strain and strain-rate. Stiffness was calculated by dividing the force from indentation area and by displacement divided by the cartilage's original thickness. The average stiffness of samples and the upper SD are indicated in the figure.
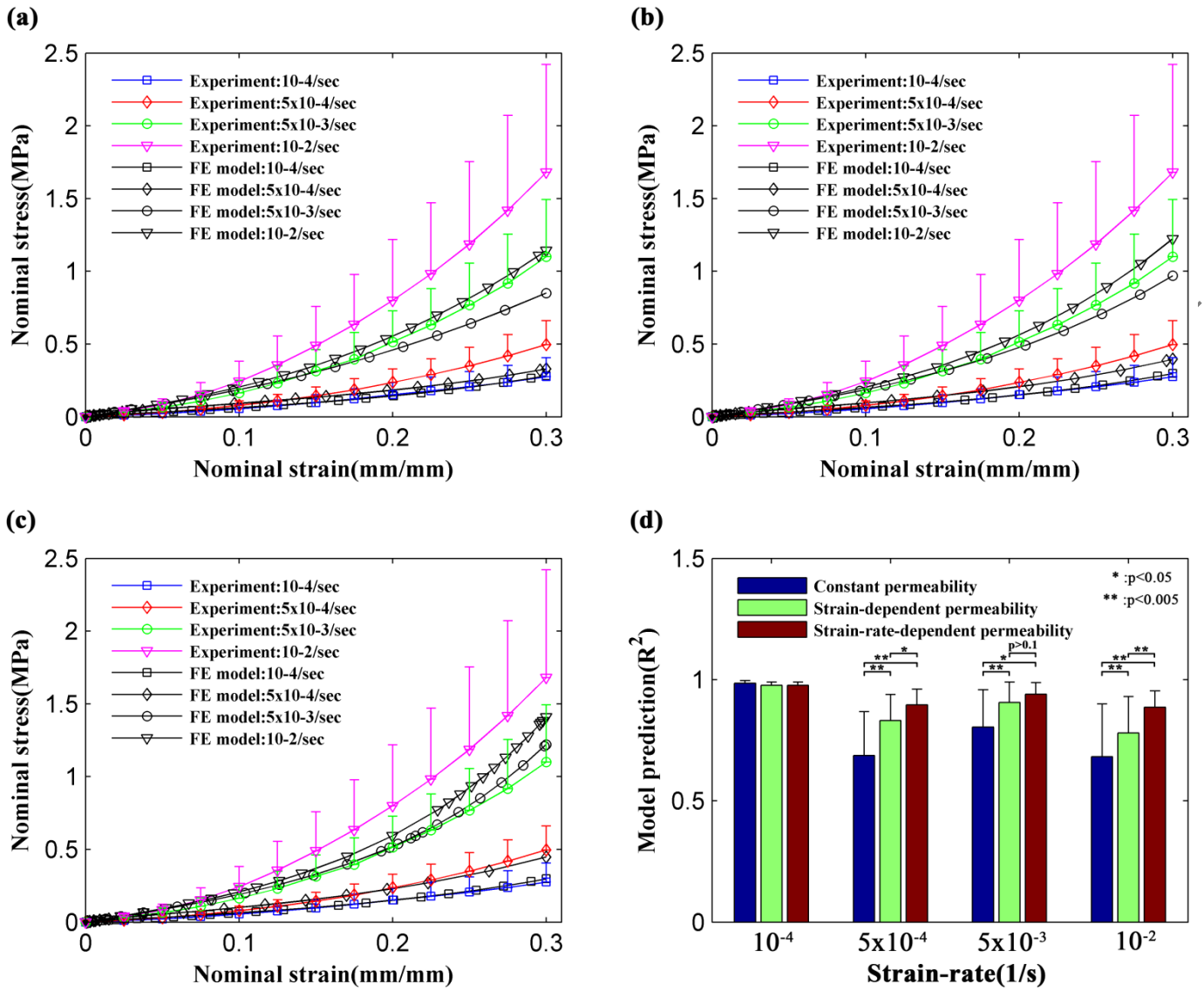
Fig. 3 Comparison of FE model prediction to average results of mechanical indentation tests of 10 samples **(a)** Model with constant permeability **(b)** Model with strain-dependent permeability **(c)** Model with strain-rate-dependent permeability **(d)** Model predictions in terms of R-squared (R^2) values and the corresponding significant differences among constant, strain-dependent and strain-rate-dependent models at individual strain-rate.

(a)

```
+1.2D
+1.1D
+1.DD
+9.DD
+8.DD
+7.DD
+6.DD
+5.DD
+4.DD
+3.DD
+2.DD
+1.DD
+0.DD
```

(b)

(c)
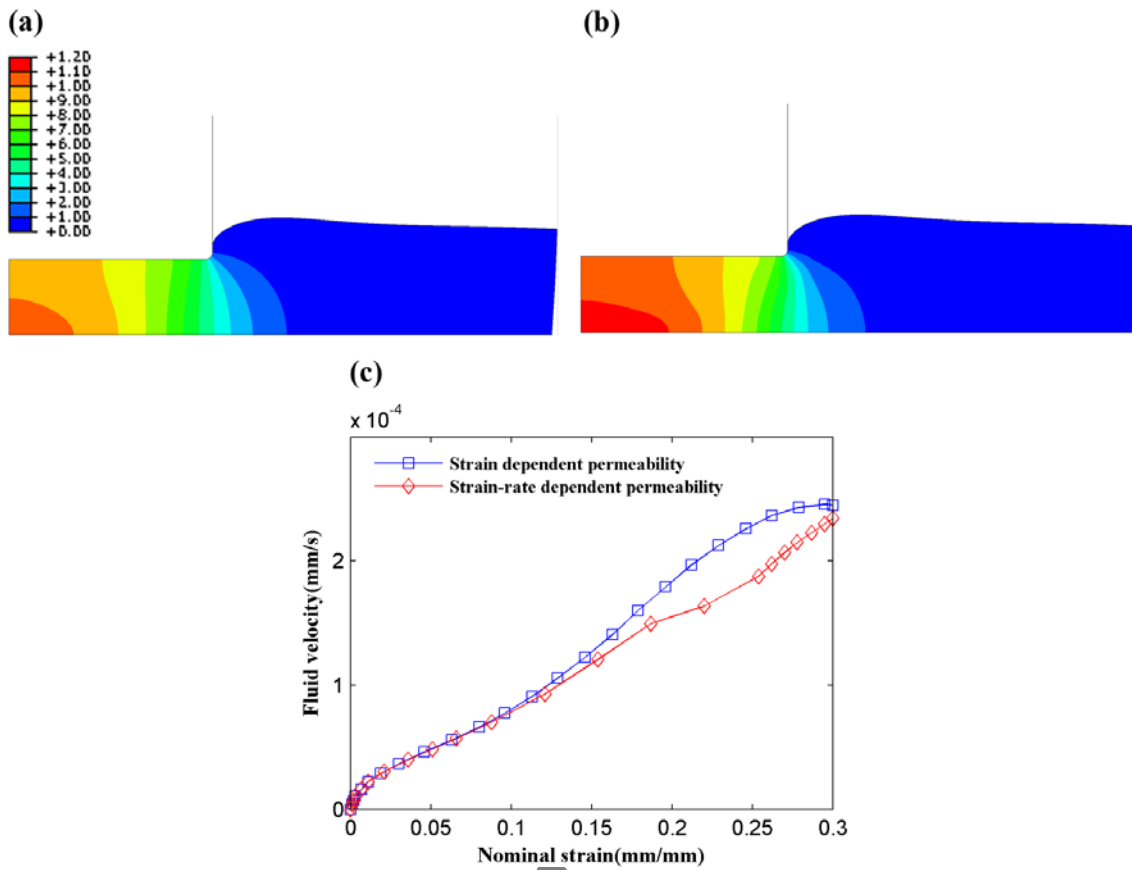
Fig. 4 Comparison of pore-pressure and velocity profiles at 10^{-2}/s **(a)** strain-dependent model **(b)** strain-rate-dependent model **(c)** fluid velocity at the bottom left of cartilage matrix.

37